Supporting Information

for

Origami – Inspired, On-Demand Deployable and Collapsible Mechanical Metamaterials with Tunable Stiffness

Zirui Zhai[1], Yong Wang[2], and Hanqing Jiang[1,#]

[1]School for Engineering of Matter, Transport and Energy, Arizona State University, Tempe, AZ 85287, USA

[2]Department of Engineering Mechanics, Zhejiang University, Hangzhou, Zhejiang 310027, China

#Email: Hanqing.Jiang@asu.edu

Justification of modeling origami structures using truss models

In this paper, truss models are used to model origami structures. In a recent paper[1], detailed comparisons have been conducted to justify the application of truss models to origami structures. Here, we specifically performed finite element simulations on triangular patterns subjected to characteristics deformations, namely, in-plane stretching, in-plane shearing, and out-of-plane bending. The finite element simulations were compared with the results using the truss model. **Figure S1** shows the results and here the normalization is through the maximum displacement in each case. As seem in these three loading cases, the truss models can qualitatively agree with the finite element simulations. Specifically, for the triangulated cylinder patterns used in this study (i.e., **Figs. 1a** and **1b**), or $\gamma = 112^{\circ}$ (for **Fig. 1a**) and $\gamma = 80^{\circ}$ (for **Fig. 1b**), both tension (**Fig. S1a** and **S1b**) and shear (**Fig. S1c** and **S1d**) show excellent agreement between the finite element simulations and truss models. For bending deformation, the difference between finite element simulations and truss models is also acceptable.

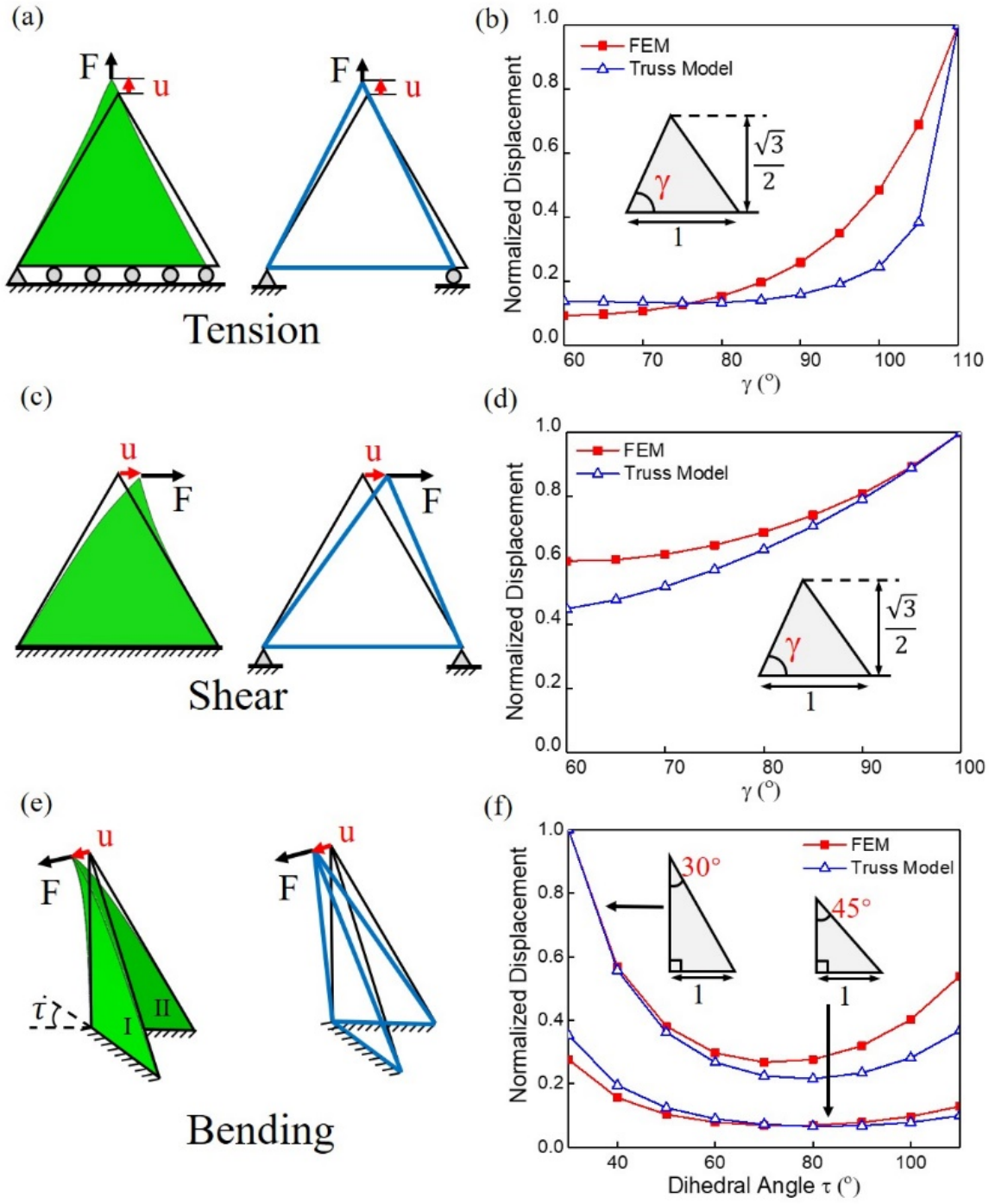

Figure S1. Comparison between finite element simulations and truss models for several featured deformation modes. ABAQUS 4-node shell elements (S4R) were used in the finite element simulations. (a) For tension, the bottom is fixed, and a concentrated force is applied at

the top vertex. **(b)** For tension, vertical displacement of the top vertex normalized by the maximum displacement for studied γ angles, as a function of γ angles. **(c)** For shear, the bottom is fixed, and a concentrated force is applied at the top vertex. **(d)** For shear, horizontal displacement of the top vertex normalized by the maximum displacement for studied γ angles, as a function of γ angles. **(e)** For bending, the bottom of two triangles with a dihedral angle τ are fixed, and a concentrated force is applied at the top vertex. **(f)** For bending, displacement of the top vertex normalized by the maximum displacement for studied dihedral angle τ, as a function of dihedral angle τ.

Geometry of triangulated cylinder patterns

Figure S2a shows a unit cell of a triangulated cylinder pattern from the crease pattern (**Fig 1a**). At the planar state,

$$L_{AB} = a\,, \tag{1}$$

and the law of sines gives

$$\frac{L_{AB}}{\sin\beta} = \frac{L_{AC}}{\sin\angle ABC} = \frac{L_{BC}}{\sin\alpha}\,, \tag{2}$$

Thus,

$$L_{BC} = a\frac{\sin\alpha}{\sin\beta} \tag{3}$$

$$L_{AC} = a\frac{\sin(\alpha+\beta)}{\sin\beta} \tag{4}$$

At the folded state, height *h*, twist angle ϕ, and radius *r* are used to characterize the geometry (**Fig. S2b**). The coordinates of the points *O*, *O'*, *A*, *B*, and *C* are given by,

$$\begin{aligned} &O\,(0,0,0), \qquad O'(0,0,h), \qquad A(r,0,0) \\ &B\left(r\cos\frac{2\pi}{n}, -r\sin\frac{2\pi}{n}, 0\right), \qquad C\left(r\cos\left(\frac{2\pi}{n}+\phi\right), -r\sin\left(\frac{2\pi}{n}+\phi\right), h\right). \end{aligned} \tag{5}$$

Then the length of the three folding lines, *AB*, *BC*, and *AC* at the folded state become

$$l_{AB} = 2r\sin\frac{\pi}{n} \tag{6}$$

$$l_{BC} = \sqrt{h^2 - 2r^2\cos\phi + 2r^2} \tag{7}$$

$$l_{AC} = \sqrt{h^2 - 2r^2\cos\left(\frac{2\pi}{n}+\phi\right) + 2r^2} \tag{8}$$

The strains in these three folding lines are

$$\varepsilon_{AB} = \frac{l_{AB} - L_{AB}}{L_{AB}} = 2\bar{r}\sin\frac{\pi}{n} - 1 \tag{9}$$

$$\varepsilon_{BC} = \frac{l_{BC} - L_{BC}}{L_{BC}} = \frac{\sin\beta}{\sin\alpha}\sqrt{\bar{h}^2 - 2\bar{r}^2\cos\phi + 2\bar{r}^2} - 1 \tag{10}$$

$$\varepsilon_{AC} = \frac{l_{AC} - L_{AC}}{L_{AC}} = \frac{\sin\beta}{\sin(\alpha+\beta)}\sqrt{\bar{h}^2 - 2\bar{r}^2\cos\left(\phi + \frac{2\pi}{n}\right) + 2\bar{r}^2} - 1 \tag{11}$$

Here $\bar{h} = \frac{h}{a}$, and $\bar{r} = \frac{r}{a}$ are normalized height *h*, and radius *r*, respectively.

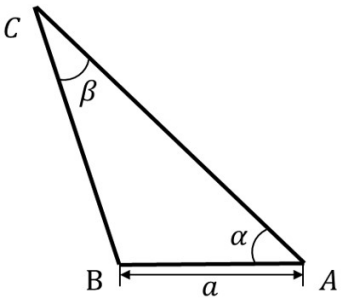

(a)

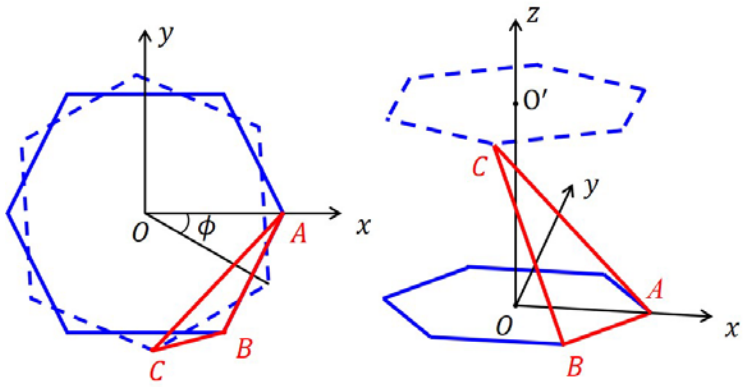

(b)

Figure S2. Illustrations of the triangulated cylinder. (a) Unit cell at the planar state, **(b)** Top view and 3D view of the folder cylindrical state.

Deformation energy analysis

For a stripe (highlighted in **Fig. 1a**), the deformation energy is given by

$$U = \frac{nEA}{2}(L_{AB}\varepsilon_{AB}^2 + L_{BC}\varepsilon_{BC}^2 + L_{AC}\varepsilon_{AC}^2) \tag{12}$$

As shown in Eqs. (9) to (11), the deformation energy U depends on three variables, namely height h, twist angle ϕ, and radius r. Using the principle of stationary potential energy, optimization with respect to these variables determines the folded states. Specifically, when only height h is prescribed, the folded state can be obtained by solving the following nonlinear equations,

$$\left.\frac{\partial U}{\partial \phi}\right|_h = \left.\frac{\partial U}{\partial r}\right|_h = 0, \qquad \left.\frac{\partial^2 U}{\partial \phi^2}\right|_h > 0, \qquad \left.\frac{\partial^2 U}{\partial r^2}\right|_h > 0\,. \tag{13}$$

When both h and ϕ are prescribed, the following equations will be solved,

$$\left.\frac{\partial U}{\partial r}\right|_{h,\phi} = 0, \qquad \left.\frac{\partial^2 U}{\partial r^2}\right|_{h,\phi} > 0\,. \tag{14}$$

MATLAB was used to solve these nonlinear equations.

Deformation energy analysis of triangulated cylinder with *n* = 6, $\alpha = 50^{\circ}$, and $\beta = 50^{\circ}$ and asymmetric tension/compression behaviors of *AC*, *AB*, or *AC* and *AB* members

In **Fig. 2c**, both *AC* and *AB* show strain variations between tension and compression during the processes of deploy and collapse. These two members are assigned asymmetrical tension and compression behavior, while *BC* truss keep a symmetrical tension and compression behavior. For *AC*, its tensile rigidity is four orders of magnitude smaller than its compressive rigidity that is as the same as that for *BC* truss. Thus, *AC* is easy to be stretched but hard to be compressed. For *AB*, its compressive rigidity is four orders of magnitude smaller than its tensile rigidity that is as the same as that for *BC* truss. Thus, *AB* is easy to be compressed but hard to be stretched. There are three combinations that can be considered in this system, specifically with just *AC* having the asymmetrical behavior, or with just *AB* having the asymmetrical behavior, or with both of them having the asymmetrical behavior. As shown in **Fig. S3**, they all show similar energy landscape with elevated energy at the collapsed state and an equilibrium state at the deployed configuration. During collapse, they all show a much higher energy barrier to prevent easy collapse. A difference is that when just *AB* truss having asymmetrical tension/compression behavior, there exists an energy barrier during deploy. Given that it is experimentally easier to achieve easy tension but hard compression, in the following study, just *AC* truss is assigned asymmetrical tension/compression behavior.

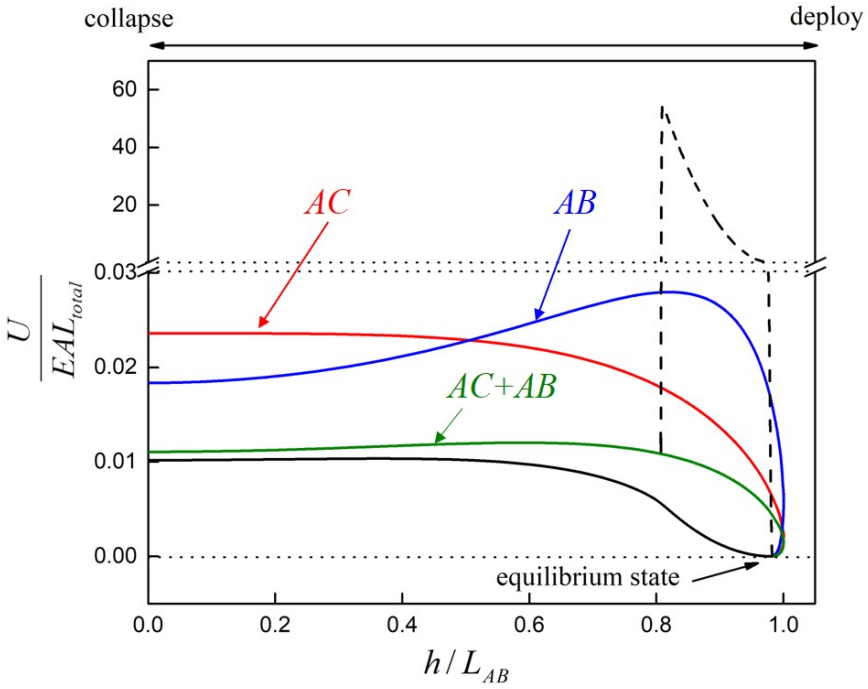

Figure S3. Energy landscape when *AC*, *AB*, or *AC* and *AB* members having asymmetrical tension and compression behavior.

Deformation energy analysis of triangulated cylinder with *n* = 4, $\alpha = 50^\circ$, and $\beta = 50^\circ$

The energy landscape and strain distribution for the triangulated cylinder with *n* = 4, $\alpha = 50^\circ$ and $\beta = 50^\circ$ are shown in **Fig. S4**. It can be seen that this pattern shows very similar feature as that for *n* = 6, $\alpha = 50^\circ$ and $\beta = 50^\circ$ (shown in **Fig. 2b**). Specifically, the completed collapsed state is at an elevated energy state and the deployed state remains at an equilibrium configuration. However, there is still an energy barrier to overcome from the collapsed to deployed states, which is similar to that shown in **Fig. 2a**. This energy barrier is about 300 times higher than that in **Fig. 2a**. For strain variations, the maximum strain exceeds 10%, such that a construction paper-folded pattern cannot be collapsed because a construction paper cannot bear this large strain. Also, similar to the strains in **Fig. 2b**, strains vary between tension and compression. For example, *AC* truss is in tension during the most of the deploy process and turns compressive right before reaching the deployed state.

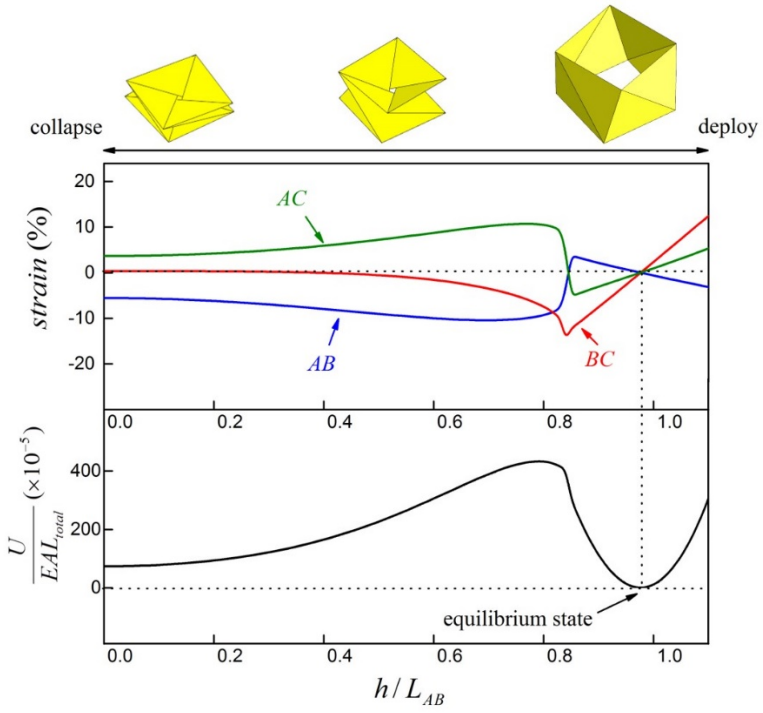

Figure S4. Energy landscapes and strain variations during the deploy and collapse processes for a pattern with *n* = 4, $\alpha = 50^\circ$, and $\beta = 50^\circ$.

Similar to **Fig. 3**, *AC* member is assigned asymmetrical tension and compression behavior. **Figure S5** shows the energy landscape, strain variations, and stiffness. This pattern again shows autonomous deploy and selective collapse as there are two collapse paths, with one for easy collapse and one for hard collapse.

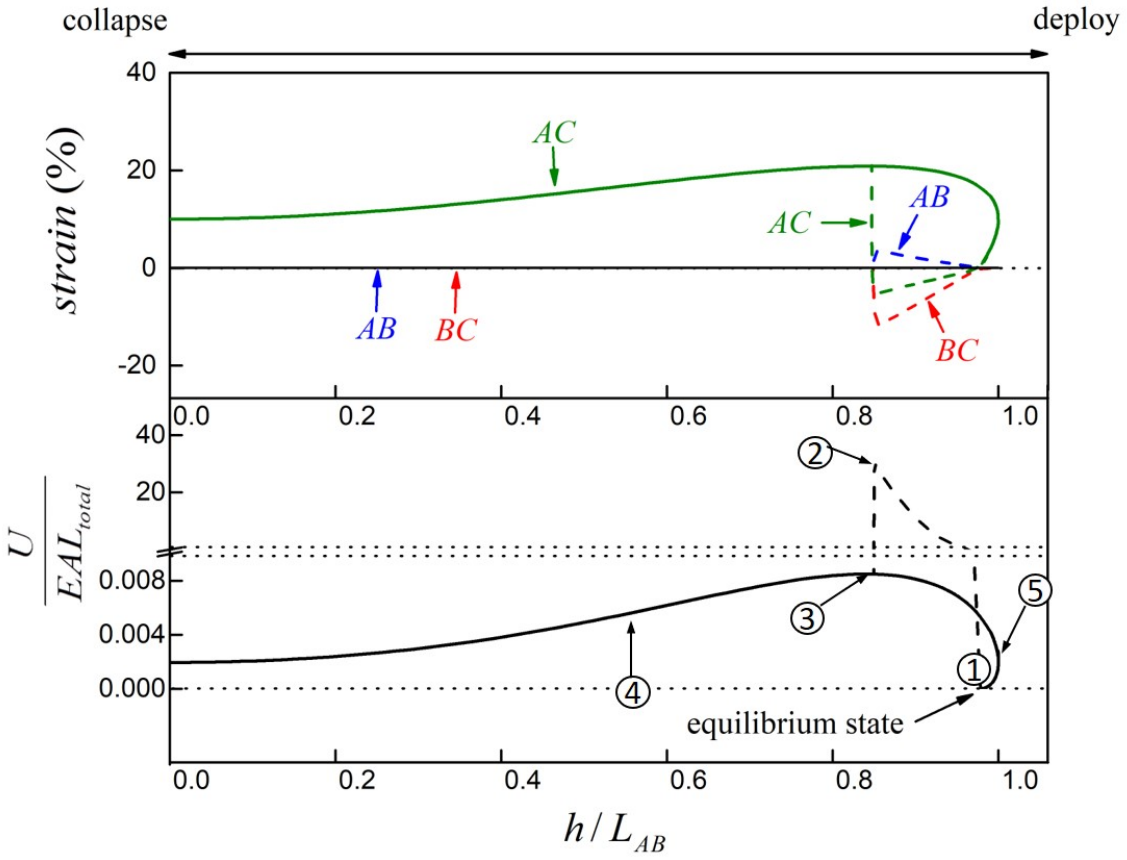

(a)

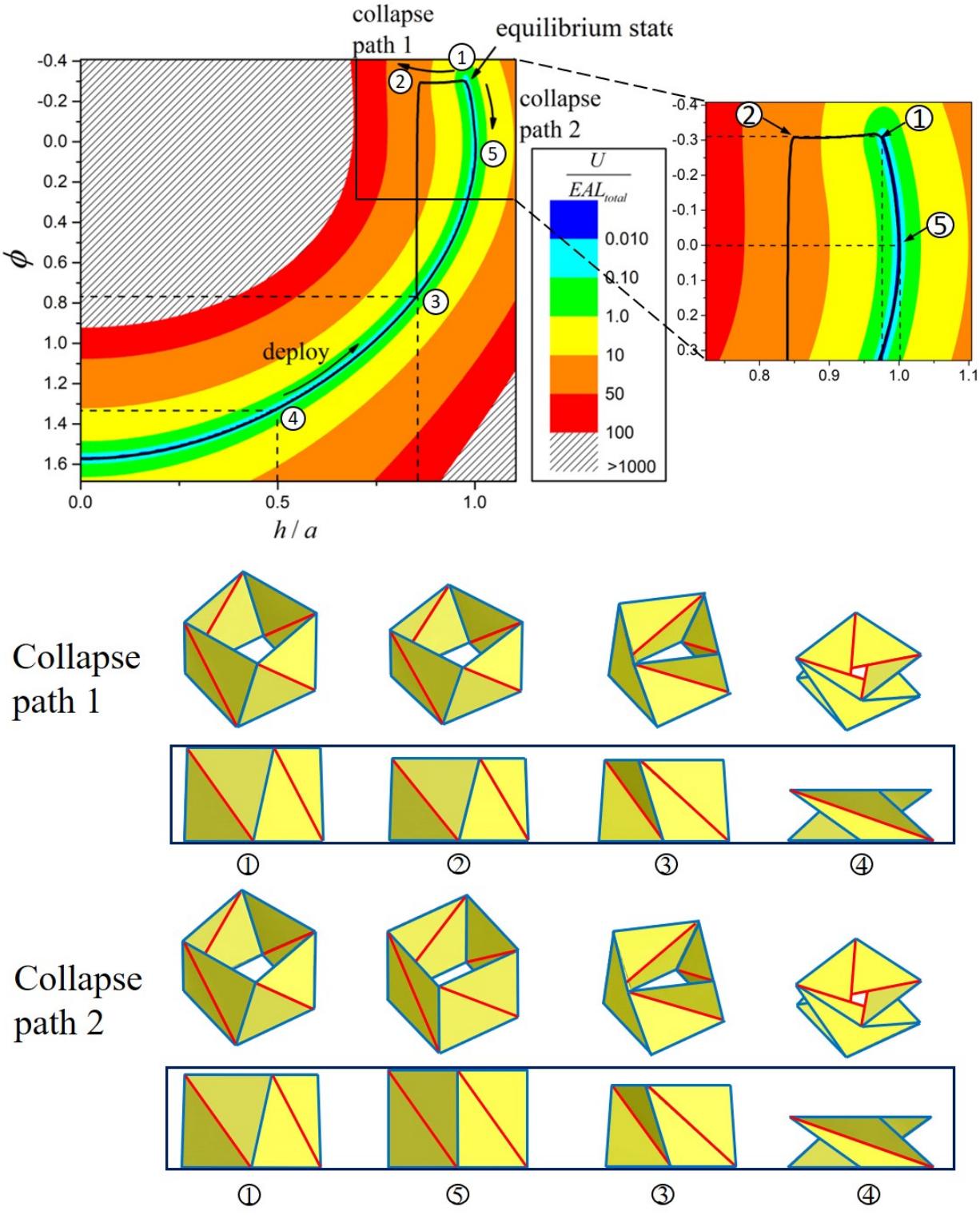
collapse
path 1
equilibrium state
collapse
path 2
deploy
ϕ
h / a
$\frac{U}{EAL_{total}}$
0.010
0.10
1.0
10
50
100
>1000
Collapse
path 1
Collapse
path 2
①
②
③
④
⑤

(b)

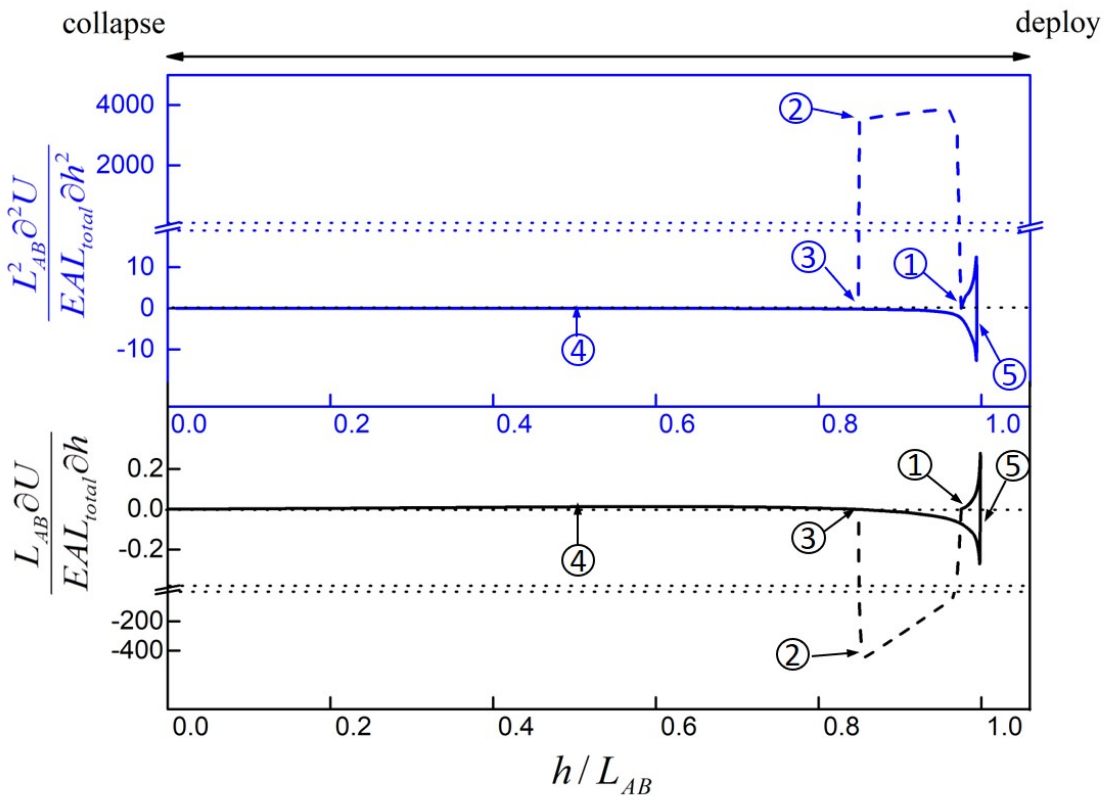

(c)

Figure S5. On-demand deployability and selective collapsibility of an origami-inspired mechanical metamaterial. (a) Energy landscapes and strain variations during the deploy and collapse processes for a mechanical metamaterial inspired by a triangulated cylinder with n = 4, $\alpha = 50^{\circ}$, and $\beta = 50^{\circ}$, and an asymmetric tension/compression behavior for *AC* member. The dashed lines are strain variations when collapsed along the path ① -> ② -> ③ -> ④, i.e., hard collapse path. **(b)** Energy contour showing two collapse paths, hard collapse path ① -> ② -> ③ -> ④ and easy collapse path ① -> ⑤ -> ③ -> ④, which suggests a selective collapse. **(c)** Tunable reaction force and stiffness of the origami-inspired mechanical metamaterial during deploy and collapse (along two paths). The dashed lines are for the hard collapse path.

Assembly of the models

No.	Description	Figure	Quantity
1	M2 × 10mm Screw	(b)	12
2	M2 × 25mm Screw	(c)	12
3	M2 × 40mm Screw	(d)	6
4	Spring	(e)	6
5	M2 Hex Nut	(f)	48
6	M4 Hex Nut	(g)	48
7	Tube 2 × 27mm	(h)	6
8	Tube 2 × 43mm	(i)	6
10	M4 × 20mm Customized	(j)	24
11	Customized PMMA	(k)	2
12	Rod End Bearing	(l)	24

(a)

(b)

(c)

(d)

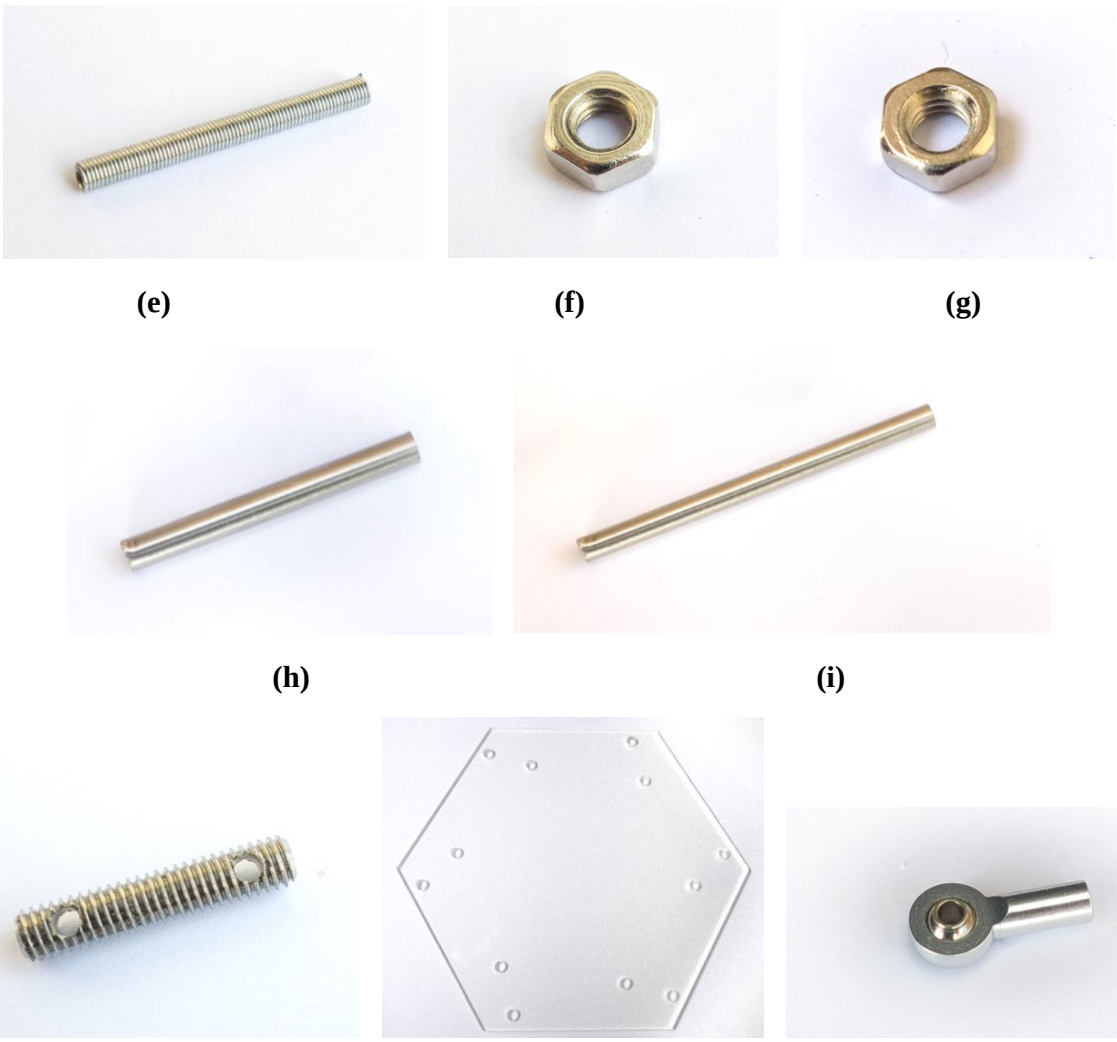

(e) **(f)** **(g)**

(h) **(i)**

(j) **(k)** **(l)**

Figure S6. List of components to build the truss-based mechanical metamaterial.

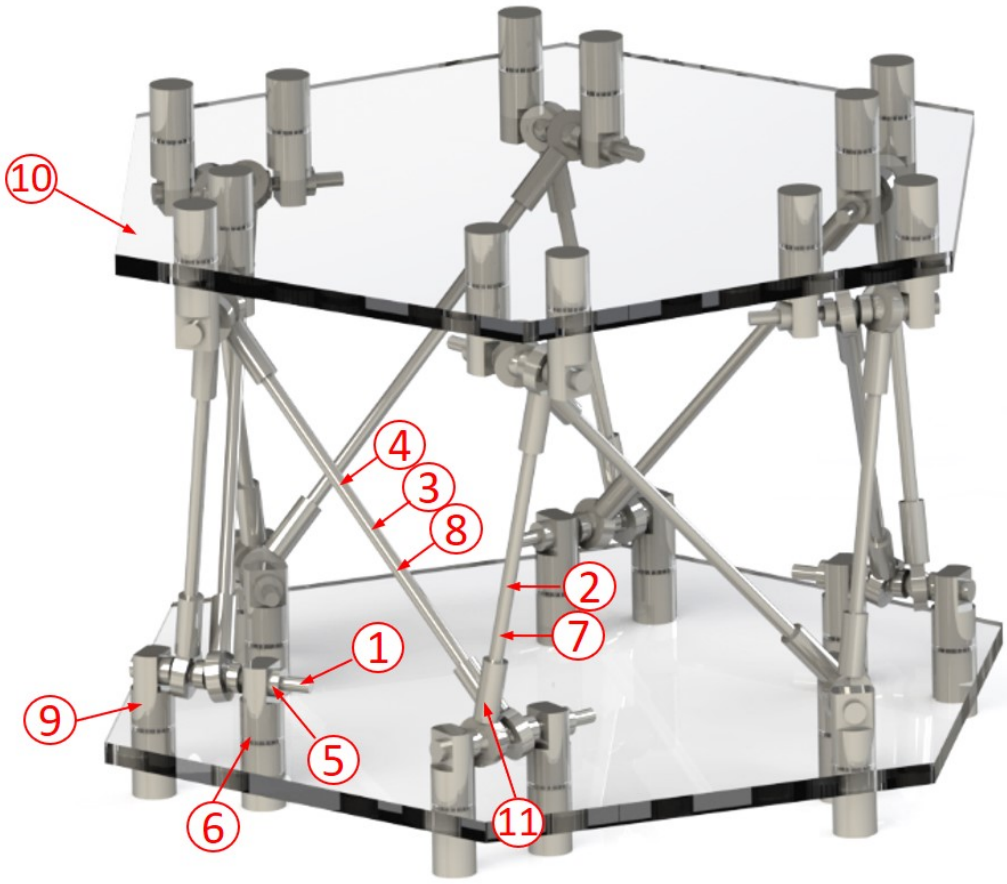

Figure S7. SolidWorks model for the truss-based mechanical metamaterial.

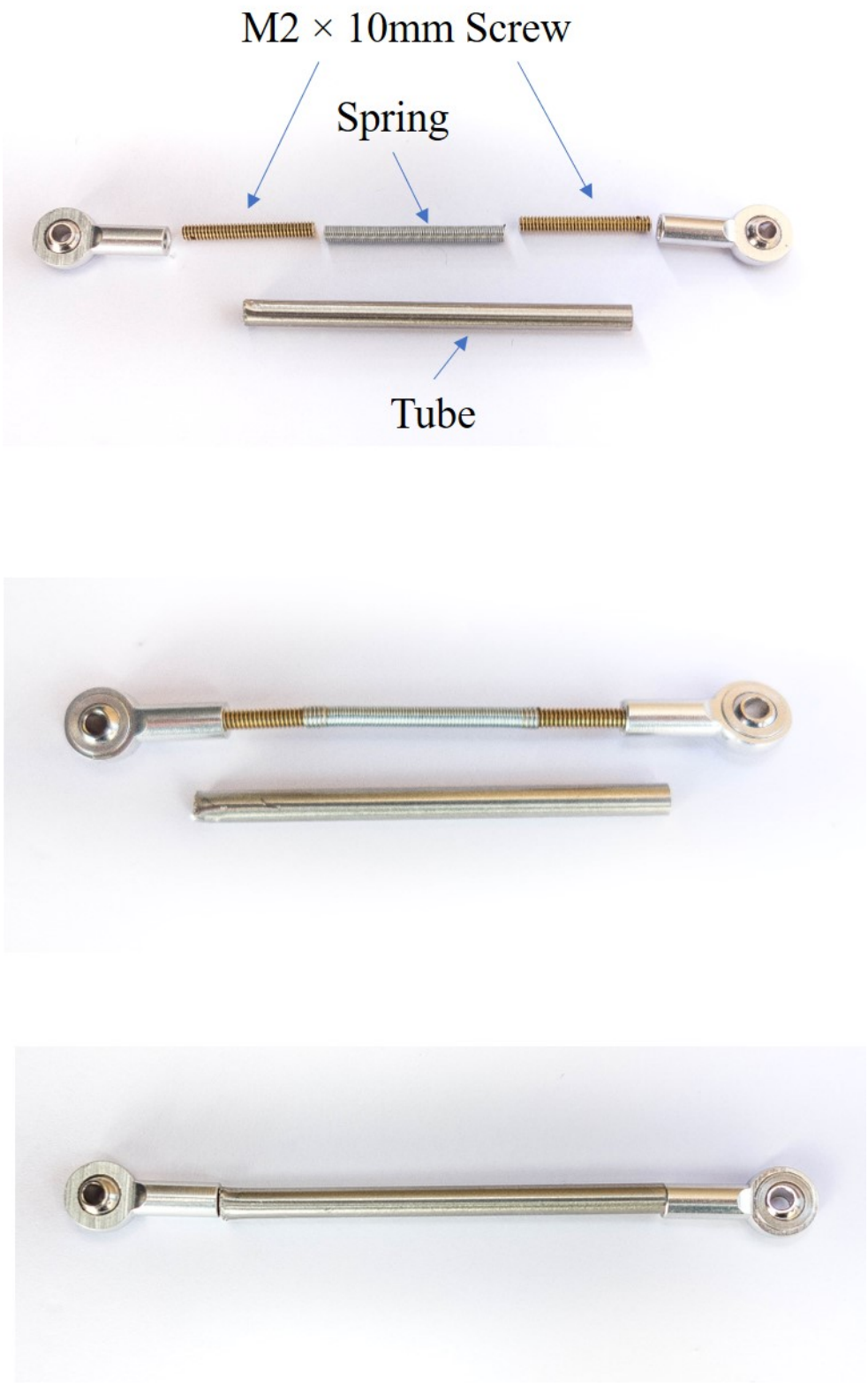

Figure S8. A spring inside a tube to achieve tension/compression asymmetry in the truss-based mechanical metamaterial.

Figure S9. Rod end bearing enables smooth rotation.

Experimental characterizations

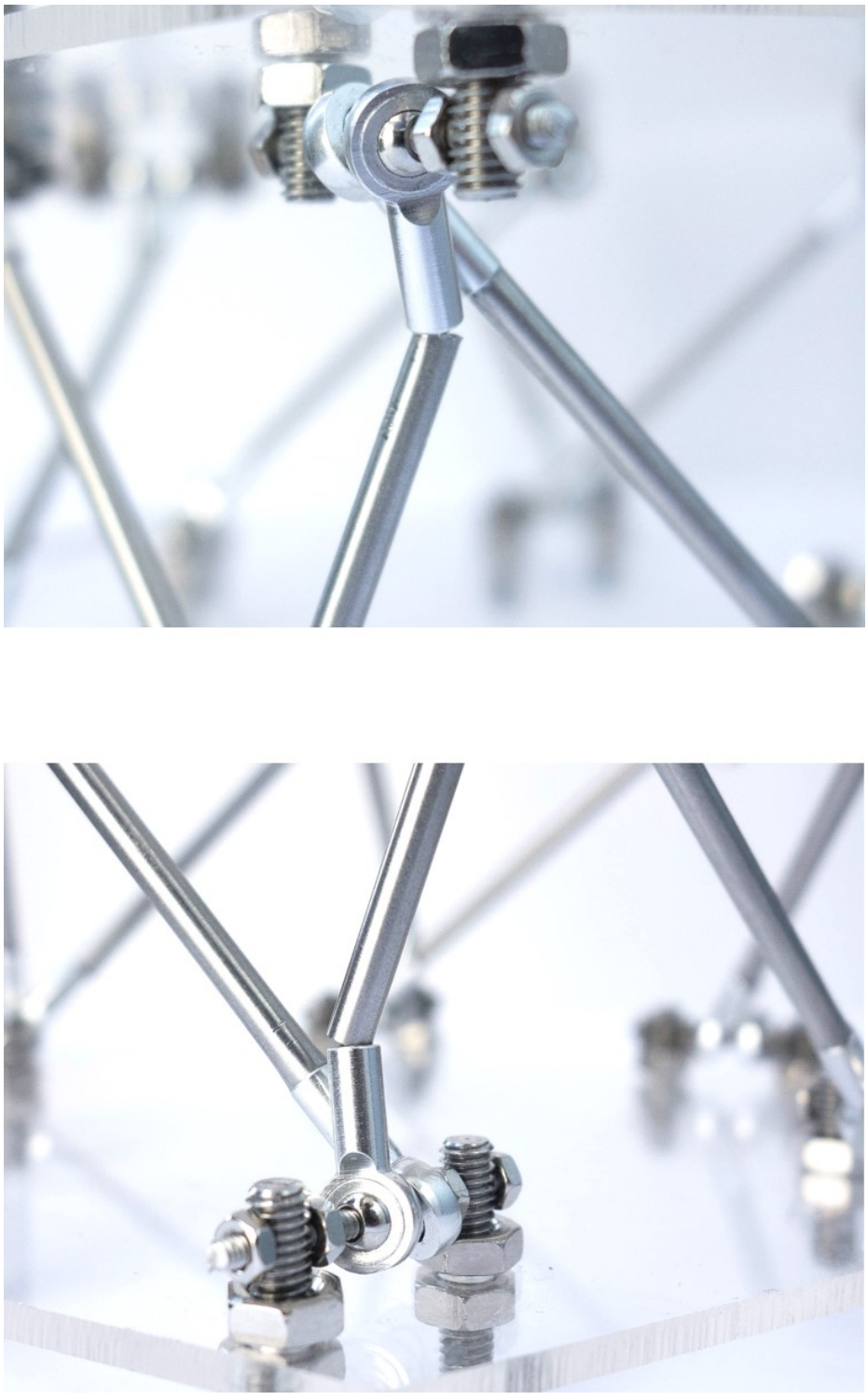

Figure S10. After compression, BC truss that bears largest compression was fractured.

(a)

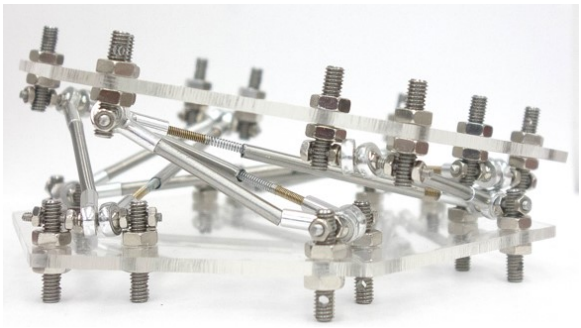

(b)

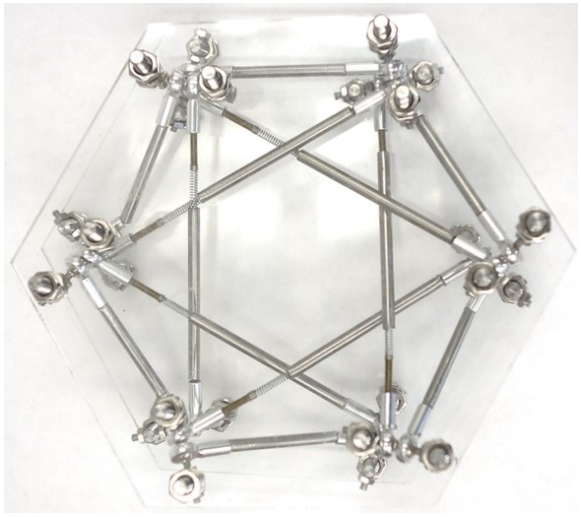

(c)

Figure S11. After the 1st compression, the metamaterial is still deployable and collapsible. (a) 3D view of the deployed state, **(b)** side view of the collapse**(c)** d view, top view of the collapsed state.

(a)

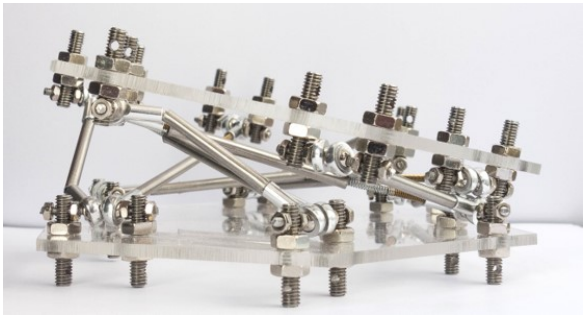

(b)

Figure S12. After the 2nd compression, the metamaterial is still deployable and collapsible. (a) 3D view of the deployed state, **(b)** side view of the collapse**(c)** d view, top view of the collapsed state.

(a)

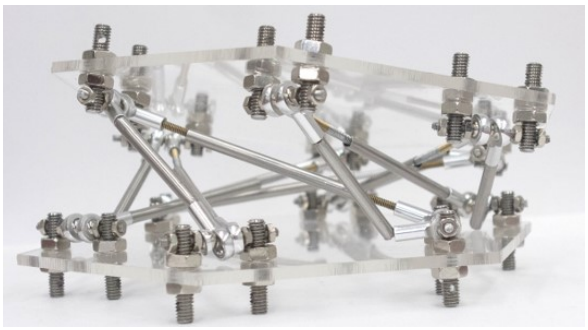

(b)

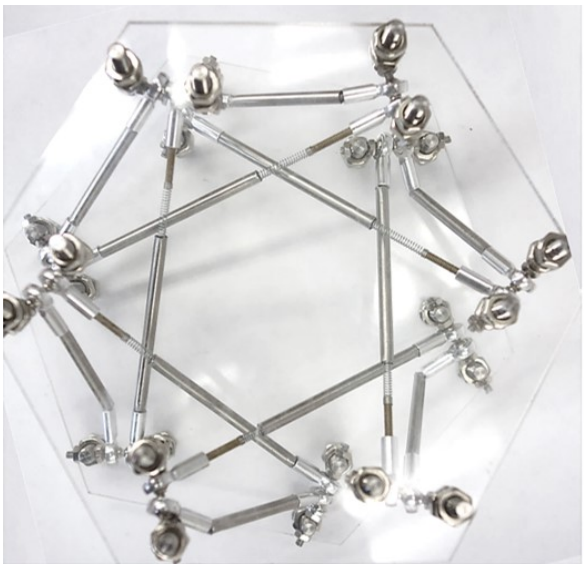

(c)

Figure S13. After the 3rd compression, the metamaterial is still deployable and collapsible. (a) 3D view of the deployed state, **(b)** side view of the collapse**(c)** d view, top view of the collapsed state.

Paper-rubber band model

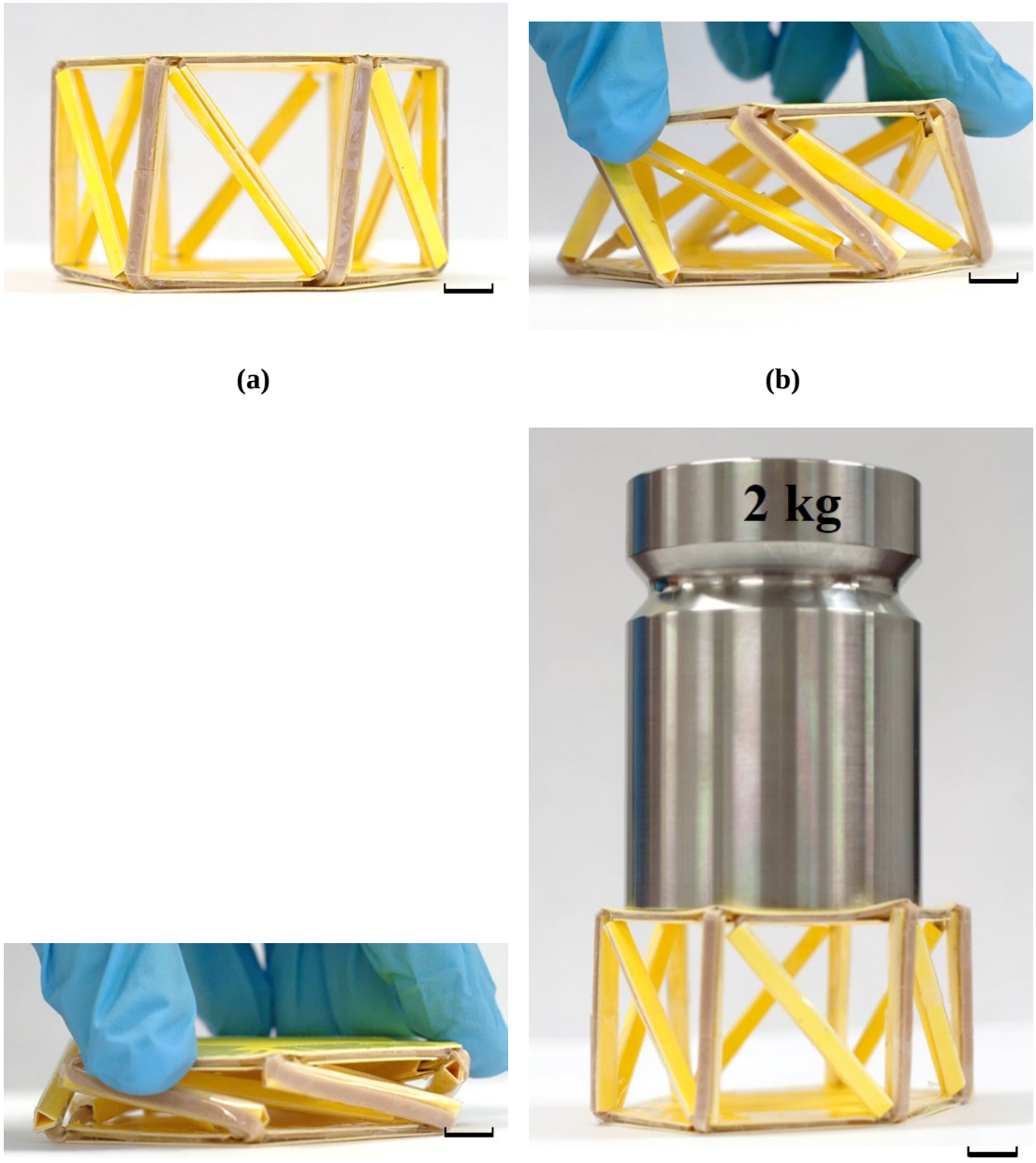

(a) **(b)**

(c) **(d)**

Figure S14. Photos for paper and rubber band based mechanical metamaterial. (a) 3D view of the deployed state. **(b)** 3D view during collapse. **(c)** 3D view of completed collapsed state. **(d)** The deployed state can bear compressive load without collapse. Scale bar is 1 cm.

Reference

1. Filipov, E. T., Liu, K., Tachi, T., Schenk, M. & Paulino, G. H. Bar and hinge models for scalable analysis of origami. *International Journal of Solids and Structures* **124**, 26-45, doi:https://doi.org/10.1016/j.ijsolstr.2017.05.028 (2017).